PCCP

PAPER

View Article Online
View Journal

Cite this: DOI: 10.1039/c6cp06943f

Thermoelectricity in transition metal compounds: the role of spin disorder†

Prashun Gorai, Eric S. Toberer and Vladan Stevanović*

Received 10th October 2016,
Accepted 1st November 2016

DOI: 10.1039/c6cp06943f

www.rsc.org/pccp

At room temperature and above, most magnetic materials adopt a spin-disordered (paramagnetic) state whose electronic properties can differ significantly from their low-temperature, spin-ordered counterparts. Yet computational searches for new functional materials usually assume some type of magnetic order. In the present work, we demonstrate a methodology to incorporate spin disorder in computational searches and predict the electronic properties of the paramagnetic phase. We implement this method in a high-throughput framework to assess the potential for thermoelectric performance of 1350 transition-metal sulfides and find that all magnetic systems we identify as promising in the spin-ordered ground state cease to be promising in the paramagnetic phase due to disorder-induced deterioration of the charge carrier transport properties. We also identify promising non-magnetic candidates that do not suffer from these spin disorder effects. In addition to identifying promising materials, our results offer insights into the apparent scarcity of magnetic systems among known thermoelectrics and highlight the importance of including spin disorder in computational searches.

1 Introduction

One of the challenges faced by computational materials science, especially in the context of materials design and computationally-guided searches for novel functional materials, is bringing theoretical predictions as close as possible to the conditions under which materials operate in target applications. For example, in solids containing transition metal atoms with localized spins, magnetic (spin) disorder can significantly affect the electronic structure properties such as density of states, effective masses, and band gaps. Consequently, the disordered (paramagnetic) phase can exhibit notably different carrier transport, optoelectronic and other relevant properties compared to its low-temperature ordered phase. Furthermore, for the majority of the known magnetic materials the transition from the low-temperature ordered phase to the high-temperature paramagnetic phase occurs around or below room temperature[1,2] as shown in Fig. 1. Thus, the electronic properties of the paramagnetic phase are the most relevant when targeting applications such as thermoelectrics, photovoltaics, and catalysis where the operating temperatures exceed typical magnetic critical temperatures.[3,4]

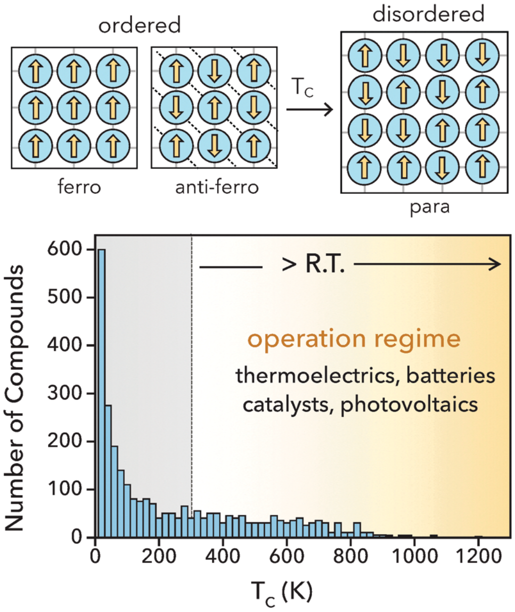

Fig. 1 Measured magnetic critical temperatures (T_c) of 2825 magnetic materials (data from ref. 1 and 2). For majority (68%) of known magnetic compounds spin disorder occurs below room temperature (R.T.).

Current computational strategies aimed at searching for novel functional materials usually rely on some choice of magnetic order when predicting the properties of solids containing transition metals. This includes either assuming a ferromagnetic spin arrangement for all considered systems,[5–7] or using the ground-state spin configuration known from experiments or approximated from first-principles calculations.[8–10] Another common approach enforces a completely non-spin polarized description of the electronic subsystem, often justified by the argument that the

---

Colorado School of Mines, National Renewable Energy Laboratory, Golden, CO 80401, USA. E-mail: Vladan.Stevanovic@nrel.gov

† Electronic supplementary information (ESI) available. See DOI: 10.1039/c6cp06943f

time- and space-average of the magnetization needs to be zero in the paramagnetic phase.[11,12] While certainly debatable, all these choices are largely driven by the desire to reduce computational expense when calculating the electronic properties across large chemical spaces. The increased computational expense stems from the need to use relatively large supercells to represent disordered states. Unlike the electronic properties, the energetics and thermodynamics of the spin subsystem, including order/disorder transitions, have been successfully modeled utilizing either model Hamiltonians, such as Heisenberg or Ising models fitted to *ab initio* total energies, or molecular dynamics simulations.[13–18] These methods can be implemented for a large number of atoms in a computationally-tractable way.

In the present work, we focus on the electronic structure and carrier transport properties of systems with localized spins in their paramagnetic phase. We demonstrate a methodology to incorporate spin-disorder in high-throughput computational searches that allows more accurate predictions at $T \gg T_c$. We begin by discussing the degree to which the electronic structure as well as the derived carrier transport properties depend on the spin configuration. Next, we show that the application of an already existing method to model lattice disorder such as the special quasi-random structure (SQS)[19] provides a reliable route for modeling the electronic structure of the paramagnetic phase. We then demonstrate that an alternative approach in which the relevant electronic structure properties are averaged over a number of random spin configurations converges to the SQS results. And finally, we implement this methodology in a high-throughput framework to assess the potential for thermoelectric performance of 1350 transition metal sulfides. We do this by using previously-developed metric (β_{SE})[20] of thermoelectric performance. The descriptor β_{SE} combines *ab initio* calculations of the bulk modulus and electronic structure parameters with semi-empirical models for electron and phonon transport to offer a reliable assessment of the intrinsic material properties that govern the thermoelectric figure of merit (zT).

Our results indicate that the value of β_{SE} changes significantly between the ground-state spin configuration and the disordered paramagnetic phase due to differences in their electronic structures. In the studied set of materials, we find that disorder usually negatively affects carrier transport, increasing effective masses and/or decreasing band degeneracies. As a result, materials which are identified as promising thermoelectrics assuming ordered spin configurations exhibit notable deterioration in their carrier transport properties in the paramagnetic phase, thereby worsening their potential for thermoelectric performance. Additionally, we identify a number of non-magnetic candidate thermoelectric materials (mainly for p-type carrier transport) that do not suffer from these spin disorder-induced renormalization effects. In addition to offering suggestions for candidate materials that deserve further experimental investigation, our findings also provide insights into the apparent scarcity of magnetic systems among the known thermoelectric materials and highlight the importance of incorporating spin disorder in computational searches.

2 Dependence of the electronic structure on spin configuration

To illustrate the strong dependence of the electronic structure on the spatial arrangement of spins, we show in Fig. 2 the calculated band structures and density of states (DOS) of an anti-ferromagnetic insulator CrN in different spin configurations. The technical details of the calculations are provided at the end under ''Computational details''. It is evident from Fig. 2 that the electronic structures corresponding to the ground state anti-ferromagnetic, hypothetical ferromagnetic and a non-magnetic (without spin) states are both qualitatively and quantitatively very different. While in the anti-ferromagnetic phase the system exhibits a finite band gap, in the ferromagnetic and non-magnetic states the gap is zero with very different density of states at the Fermi energy. The experimental results, on the other hand, indicate the existence of a finite band gap both in the low-T anti-ferromagnetic and the high-T paramagnetic phases.[21–24] This highlights the need for appropriate treatment of spin configurations when predicting the electronic properties of materials.

The strong dependence of the electronic structure on the spin configuration stems from electron–electron interactions and many-body effects, and can be illustrated using a one-dimensional Hubbard model. The 1D Hubbard model is an extension of the classic tight-binding 1D Hamiltonian with the addition of the Coulomb repulsion between electrons. In its simplest form, the Coulomb interactions are taken into account

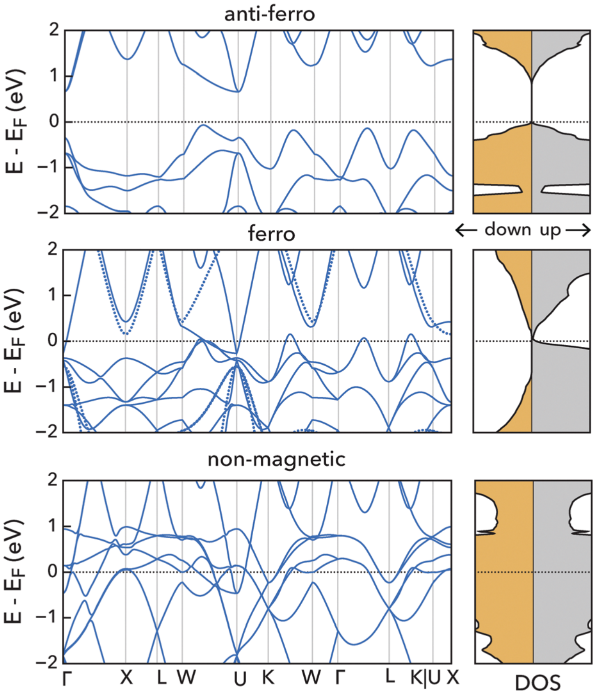

Fig. 2 DFT+U calculated band structure and density of states (DOS) of CrN in different spin configurations. The DOS is resolved into the spin-up and -down channels. The dotted line in the band structure of the ferromagnetic state denotes the spin down channel.

as an on-site energy penalty U which is incurred whenever a lattice site is doubly occupied by a spin-up and a spin-down electron. The 1D Hubbard model with nearest neighbor hopping and the on-site U repulsion‡ is usually written in the second quantization as:

$$H = -t\sum_{j,\sigma}\left(c^{\dagger}_{j,\sigma}c_{j+1,\sigma} + c^{\dagger}_{j+1,\sigma}c_{j,\sigma}\right) + U\sum_{j} n_{j,\uparrow}n_{j,\downarrow}, \qquad (1)$$

where $c^{\dagger}_{j,\sigma}$ and $c_{j,\sigma}$ represent electron creation and annihilation operators at a site j with spin σ, while $n_{j,\sigma}$ are the number operators ($n_{j,\sigma} = c^{\dagger}_{j,\sigma}c_{j,\sigma}$). We assume half filling *i.e.* one orbital and one electron per site. So, the double occupation of a certain site is penalized by U while hopping between adjacent sites is favored by the energy $-t$.

Within this model the band gap can be computed from the expectation values of the Hamiltonian given in eqn (1) as the sum of the energy $E_{N+1} - E_N$ to add an electron to the system (from vacuum), and an energy $E_{N-1} - E_N$ to remove an electron from the system (to vacuum), *i.e.*,

$$E_g = [E_{N+1} - E_N] + [E_{N-1} - E_N]. \qquad (2)$$

Then, if one assumes ferromagnetic order, *i.e.* every site occupied by a spin up electron, then adding a spin down electron to a given site would cost U. Because the added electron is allowed to hop to neighboring sites there will also be a negative $-2t$ contribution as shown schematically in Fig. 3. The energy to add an electron would then be $E_{N+1} - E_N = U - 2t$ (Fig. 3). If a spin up electron is removed from a certain site, the net $E_{N-1} - E_N = -2t$ is gained because the neighboring electrons are now allowed to hop to the vacant site. Hence, the band gap of the ferromagnetic state becomes $E_g^{\mathrm{FM}} = U - 4t$. On the other hand, if one assumes an anti-ferromagnetic order with anti-parallel spin alternating on adjacent sites, adding an electron in any spin direction costs U and removing one costs $+2t$ as the hopping energy of the removed electron is lost. Therefore, the band gap is $E_g^{\mathrm{AFM}} = U + 2t$. Finally, in the fully random (paramagnetic) phase, every site will have, on average, one spin-up and one spin-down neighbor resulting in $E_g^{\mathrm{para}} \approx U - t$.

It becomes clear from this simple example that the interplay between electron–electron repulsion (U) and hopping (t) is responsible for the dependence of the electronic structure on the spin configuration. In the atomic limit ($t = 0$) or independent electron approximation ($U = 0$), this dependence does not exist resulting in $E_g = U$ and $E_g = 0$, respectively, regardless of the spin configuration. Furthermore, this example also illustrates the significant differences in the density of states between the ferromagnetic and anti-ferromagnetic configuration – in the former case, electrons can be removed only from spin up states (spin down DOS close to the valence band maximum is zero) or added only to spin down states (spin up DOS close to the conduction band edge is zero), while in the anti-ferromagnetic configuration, there is no such constraint. Consequently, DOS effective masses and the related transport properties will also vary depending on the spin configuration. The situation is much more complicated in real 3D systems with multiple bands, but as long as the band edges are formed of d- or f-atomic orbitals, the resulting electronic structure will strongly depend on spin configuration as demonstrated in Fig. 3.

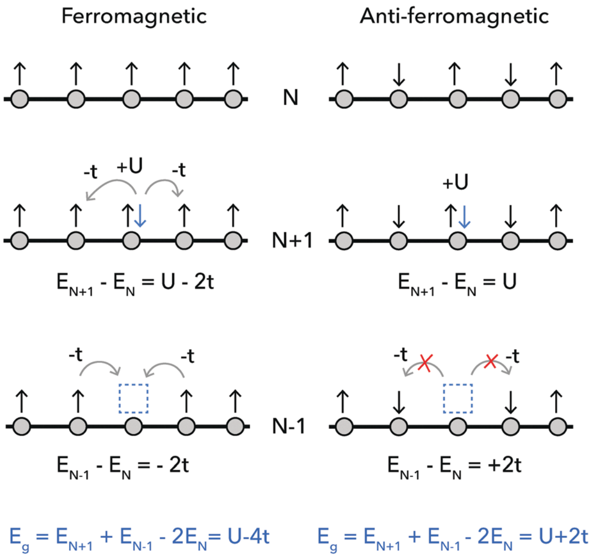

Fig. 3 Schematic of the differences in the band gap (E_g) between the ferromagnetic and anti-ferromagnetic states as described by a 1D Hubbard model. It is the interplay between the onsite Coulombic repulsion (U) and hopping (t) that leads to differences in the electron addition (E_{N+1}) and removal energy (E_{N-1}) between the two states.

3 Approach to modeling the electronic structure of the paramagnetic phase

It has been previously argued that the most appropriate way to describe the paramagnetic state of an insulator or a strongly-correlated metal is by utilizing many-body approaches such as the dynamical mean field theory (DMFT)[25,26] that offers treatment of fluctuating spins. While certainly successful in describing certain classes of strongly correlated systems that are largely inaccessible to standard DFT, the primary limitation of DMFT is its computational cost, which at present prevents it from being implemented for broad material searches.

When using atomistic methods such as DFT or DFT+U, which require initializing local moments on the atoms at the beginning of the calculation, the most important component is the realization of the spin configuration that best approximates the random spin arrangement of the paramagnetic state. To date, several approaches have been developed for this purpose.[27] Within the *ab initio* DFT-based molecular dynamics, Antropov *et al.* introduced the adiabatic spin approximation[28,29] that treats spin dynamics explicitly. The more widely used methods are based on the supercell approach, such as disordered local moments in the coherent potential approximation (DLM-CPA)[30,31] and spin-wave method,[32] which was introduced recently. In addition to the computational cost, another disadvantage of methods such

---

‡ The energy of an atomic orbital that enters both the tight-binding and the Hubbard model is assumed to be zero.

as DLM-CPA is that local structural relaxations cannot be performed.[27]

Here we approximate the paramagnetic state with the fully random spin configuration, which we model by utilizing special quasi-random structures (SQSs).[19] Strictly speaking this corresponds to the infinite temperature limit[33] and is appropriate given the rather low values of magnetic critical temperatures of most materials (Fig. 1). Mathematically, the SQS represents a spin arrangement constructed on a finite supercell that best matches a spin–spin correlation function of a fully random spin structure. The paramagnetic state is characterized by the vanishing of the average spin–spin correlation function:[34]

$$\langle \Phi_\alpha \rangle = \frac{1}{N} \sum_{i,j \in \alpha} \boldsymbol{e}_i \cdot \boldsymbol{e}_j = 0, \forall \alpha \qquad (3)$$

where N is a normalization factor, α goes over the coordination shells, and $\boldsymbol{e}_i$ are the unit vectors along the spin quantization axis on atomic site i. A supercell with magnetic moments that satisfy eqn (3) is a suitable candidate for modeling the high-temperature paramagnetic phase. Even though in the actual paramagnetic state the magnetic moments are non-collinear and dynamic, a supercell with static collinear spins is appropriate as long as the pair-wise parallel and anti-parallel spin correlations cancel each other,[34] resulting in $\langle \Phi_\alpha \rangle = 0$.

It has been shown that a special quasi-random structure (SQS)[19] for the magnetic moments in a supercell can be used to model the magnetic disorder in the high-temperature paramagnetic phase, with the constraint that the spin-up and spin-down magnetic moments exactly cancel each other.[27,34] The SQS methodology has been successfully employed to model chemical disorder in alloys[35–38] as well as the spin–spin interactions and the thermodynamics of the spin disorder.[16] Previous work has shown that the magnetic SQS approach within the DFT+U scheme gives total energies and lattice constants that are similar to the DLM-CPA method and provides a good description of the equation of state (energy *vs.* volume) and the density of states of 3d transition metal compounds.[27,34] In this work we use the magnetic SQS of the paramagnetic phase as the input to DFT+U electronic structure calculations, which we use to obtain carrier transport parameters such as DOS effective masses and band degeneracies. It is important to keep in mind that the magnetic SQS is a "frozen" spin picture of the magnetic disorder and does not account for spin dynamics, which can affect carrier transport through the electron–magnon type of interactions. These effects are beyond the scope of this paper; the primary focus here is on predicting the renormalization of the electronic structure and related properties due to spin disorder.

As an alternative to SQSs, the property of interest in the paramagnetic phase can be obtained by averaging the property over a sufficient number of supercells with randomly-distributed magnetic moments such that the net magnetic moment in the supercell is zero.[34] We refer to these supercells with randomly-distributed moments as random samples (RSs). We show that the RS total energies and relevant electronic structure parameters converge to those of the SQS. Even though the number of DFT calculations to be performed in the RS approach increases, it is particularly attractive because it bypasses the need to perform the Monte Carlo-based simulated annealing, typically used to generate an SQS structure.[39] Details of the RS are provided at the end under "Computational details".

Case examples

Here, we showcase our approach on two material systems (CrN, MnSe) and compare and contrast the energies and the relevant electronic structure parameters of different ordered spin configurations and the high-T paramagnetic phase modeled using a magnetic SQS. Both systems order anti-ferromagnetically below the Néel temperatures of ∼280 K and ∼130 K for CrN and MnSe, respectively.[11,34,40] Fig. 4 and 5 show the calculated total energies and electronic structure parameters for the ground-state anti-ferromagnetic (AFM) phase, hypothetical ferromagnetic (FM) phase (dashed line), and the paramagnetic state approximated by a spin SQS structure. In addition, the distribution of the results for 20 random samples (RS) is plotted as a histogram. Our calculations correctly identify the known anti-ferromagnetic ground state as the lowest-energy spin state for both systems. The energy per atom increases from the anti-ferromagnetic to the SQS to the ferromagnetic state, confirming the hypothetical nature of the ferromagnetic state for these two systems (energy above disordering). The energy distribution of random samples averages to within 1 meV per magnetic atom from the SQS.

Next, we analyze how the electronic structure parameters that enter β_{SE}, the descriptor for thermoelectric performance, vary between different spin states. These include density of states effective mass ($m_{\mathrm{DOS}}{}^*$) and band degeneracy (N_{b}) for each band edge. N_{b} counts the number of carrier pockets or valleys close to the valence and conduction band edge. While DFT and DFT+U are known to underestimate the band gaps, $m_{\mathrm{DOS}}{}^*$ and N_{b} are reproduced with sufficient accuracy to correctly identify the known thermoelectric materials using the metric β_{SE}.[20,41]

We disqualify the ferromagnetic states from further discussion because their energies lie above the energy of the SQS, and they exhibit zero band gaps (Fig. 4 and 5). When the electronic structure of the anti-ferromagnetically ordered state is compared with that of the SQS and the RS the following trends emerge: (1) in the case of CrN (Fig. 4) the disorder increases $m_{\mathrm{DOS}}{}^*$, more so for the conduction than for the valence band, and decreases N_{b}, more for the valence than for the conduction band, and (2) the results for MnSe follow similar trends with the largest effect of disorder being almost an order of magnitude increase in the valence band $m_{\mathrm{DOS}}{}^*$ with band degeneracies being fairly similar to those of the AFM state with only a slight increase (decrease) between different spin configurations for the valence (conduction) bands.

It is important to note that the SQS and average of random samples ($\langle \mathrm{RS} \rangle$) are sufficiently close to each other such that either approach can be used for the purpose of materials

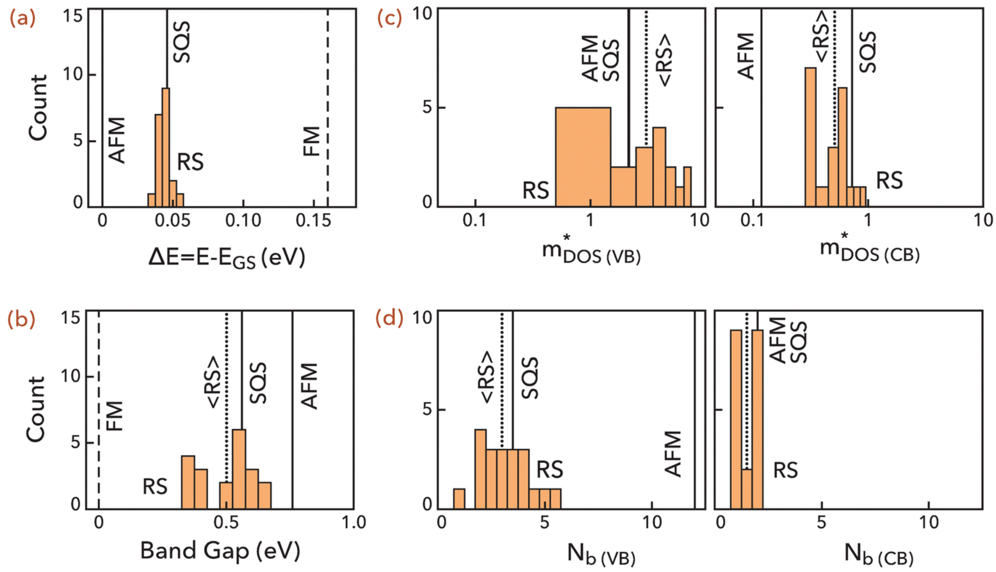

Fig. 4 Calculated (a) energies above ground-state ΔE, (b) band gaps, (c) density of states effective masses m_{DOS}*, and (d) band degeneracies N_{b} of ferromagnetic (FM), anti-ferromagnetic (AFM), special quasi-random structure (SQS), random samples (RS), and average of random samples (⟨RS⟩) for CrN. The random samples are shown as a histogram. m_{DOS}* and N_{b} are shown for valence and conduction bands.

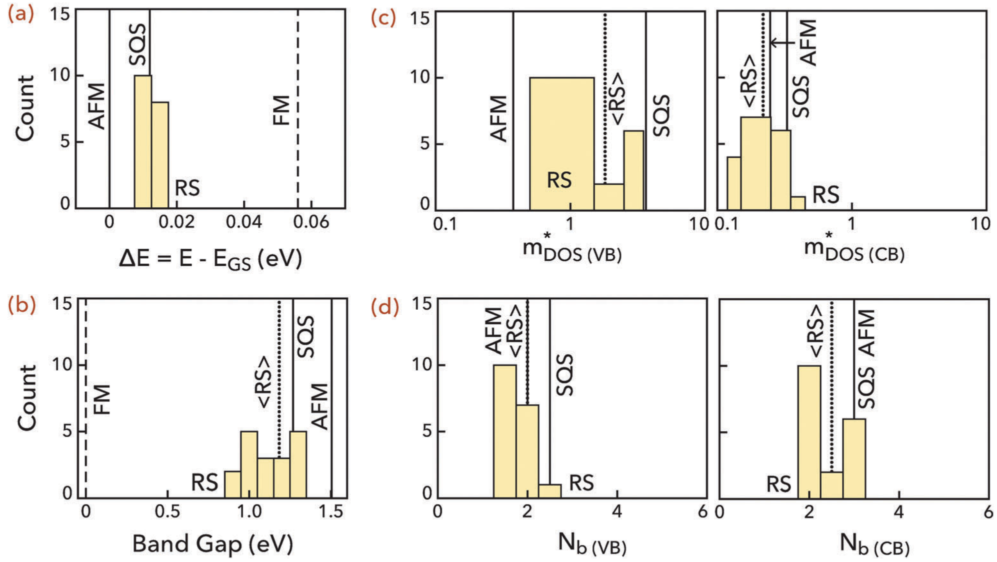

Fig. 5 Calculated (a) energies above ground-state ΔE, (b) band gaps, (c) density of states effective masses m_{DOS}*, and (d) band degeneracies N_{b} of ferromagnetic (FM), anti-ferromagnetic (AFM), special quasi-random structure (SQS), random samples (RS), and average of random samples (⟨RS⟩) for MnSe. The random samples are shown as a histogram. m_{DOS}* and N_{b} are shown for valence and conduction bands.

screening. Judging from these two cases, it appears that spin disorder deteriorates the charge transport properties – by increasing effective masses or decreasing band degeneracies or both. Based on the 1D Hubbard model from Section 2, disorder in the anti-ferromagnetic state will limit the otherwise perfect hopping between adjacent sites and lead to heavier masses. The trends in N_{b} are much less intuitive. Effects of local symmetry breaking, both translational and point group, can lift the energy degeneracy of different valleys, while establishing higher global symmetry could imply an increase in band degeneracy. The balance of these two effects is what determines the final values.

4 Application: carrier transport and thermoelectric performance of transition-metal sulfides

We employ the described procedure to assess the charge transport properties and potential for thermoelectric performance of transition-metal sulfides in their paramagnetic phase. In general, materials with a large figure of merit zT are desired for thermoelectric applications. zT is expressed as,

$$zT = \frac{\alpha^2 \sigma T}{(\kappa_e + \kappa_L)}, \tag{4}$$

where α is the Seebeck coefficient, σ the electronic conductivity, and κ_e and κ_L the electronic and lattice components of thermal conductivity.[3] Consideration of the Boltzmann transport equations for α, σ and κ_e in the relaxation time approximation[42] yields an expression

$$zT = \frac{u\beta}{(v\beta + 1)}, \tag{5}$$

where u and v depend on charge carrier chemical potential (η) and carrier scattering mechanisms, and β is a material-dependent parameter (known as the quality factor). Therefore, maximizing zT requires simultaneously optimizing the intrinsic material properties, contained within β, as well as doping. The parameter β is defined as:

$$\beta = \frac{2e}{\hbar^3}\left(\frac{k_B}{e}\right)^2\left(\frac{k_B}{2\pi}\right)^{3/2}\frac{\mu_0 m_{DOS}{}^{*3/2}}{\kappa_L}T^{5/2} \tag{6}$$

where μ_0 is the intrinsic charge carrier mobility, $m_{DOS}{}^*$ the density of states (DOS) effective mass, κ_L the lattice thermal conductivity, k_B the Boltzmann constant, e the electronic charge and $\hbar$ the reduced Planck constant. For optimally doped materials that maximize zT, the β value calculated from measured room temperature μ_0, $m_{DOS}{}^*$ and κ_L is found to be a good descriptor of the maximum achievable zT, as demonstrated in ref. 20. To address the challenges associated with direct calculation of the transport properties entering eqn (6), we have recently developed semi-empirical models for μ_0 and κ_L[20] by combining first-principles calculations and a large body of measured room temperature μ_0 and κ_L for a range of materials. Using these semi-empirical models, β (now referred to as β_{SE}) can be evaluated from first-principles calculations and in a high-throughput fashion.

The model for mobility is motivated by the classic electron–phonon scattering models,

$$\mu_0 = A_0(B)^s(m_b{}^*)^{-t}, \tag{7}$$

where B is the bulk modulus, $m_b{}^*$ the band effective mass, and A_0, s, and t are fitting parameters. Similarly, the lattice thermal conductivity (κ_L) is derived from the Debye–Callaway model as

$$\kappa_L = A_1\frac{\bar{M}v_s{}^3}{V^{2/3}n^{1/3}} + A_2\frac{v_s}{V^{2/3}}\left(1 - \frac{1}{n^{2/3}}\right) \tag{8}$$

where $\bar{M}$ is the average atomic mass, V the average volume per atom, v_s the speed of sound, and n the number of atoms in the primitive cell. A_1 and A_2 are fitting constants in the model. To a first approximation, v_s depends on B and density d $\left(v_s = \sqrt{B/d}\right)$. In the paramagnetic phase, phenomena such as magnon–phonon scattering can lower the lattice thermal conductivity but for the present purposes can be assumed to be a second-order effect that will be masked by large changes in the charge transport properties. We assume that κ_L remains largely unchanged between the ordered magnetic and disordered paramagnetic phase.

Therefore, to evaluate β_{SE} one needs to compute $m_{DOS}{}^*$, band effective mass ($m_b{}^*$), and bulk modulus (B). Other parameters entering β_{SE} are also directly accessible from these calculations. The band effective mass ($m_b{}^*$) is evaluated from $m_{DOS}{}^*$ and the band degeneracy (N_b), using the relation $m_{DOS}{}^* = N_b{}^{2/3}m_b{}^*$. N_b is the total number of bands in all charge carrier pockets close to the band edge across the entire first Brillouin zone. N_b is calculated from the electronic structure using our previously-developed algorithm.[20] In the context of evaluating β_{SE}, the electronic structure parameters that are of primary interest are $m_{DOS}{}^*$ and N_b. Although β_{SE} does not explicitly depend on the value of the bandgap (E_g), it is an important electronic structure parameter that governs the onset of the bipolar heat transport in thermoelectric materials. In the case examples, we examined the changes in total energies and electronic structure properties (E_g, $m_{DOS}{}^*$, N_b) in going from the ground state to the paramagnetic phase. Now we apply the same procedure to compute β_{SE} for 1350 transition-metal sulfides.

The 1350 structures from the Inorganic Crystal Structure Database (ICSD)[43] contain 3d-block transition metals (excluding only Tc, Ru, Rh) and less than 50 atoms in the primitive cell. In order to calculate $m_{DOS}{}^*$ and N_b, a system should have a finite band gap. Therefore, for every structure we first perform a limited search for the lowest-energy spin configuration on the ICSD primitive unit cell and compute β_{SE} for only those structures that have a finite DFT+U band gap in their lowest-energy spin configuration. Out of the 1350, only 600 structures have a non-zero DFT+U band gap. We then calculate β_{SE} for these 600 materials in their lowest-energy spin configuration. The procedure adopted for finding the lowest-energy spin configuration is discussed in section "Computational details". The data for these 600 sulfides are available in our open-access database (wwww.tedesignlab.org)[44] as well as in the ESI† (Table S1). We find that a large fraction of these 600 materials are non-magnetic, *i.e.* the spin density is equal to zero implying a low-spin state of the transition metals.

Fig. 6 shows the variation in β_{SE} with the calculated band effective mass ($m_b{}^*$) and lattice thermal conductivity (κ_L) for the 600 sulfides with non-zero band gaps. The bubble area scales with the value of β_{SE} for conduction (Fig. 6a) and valence (Fig. 6c) band transport *i.e.* for assumed p- and n-type materials, respectively. Candidate materials that are magnetic (non-zero magnetic moment) in their lowest-energy state and are predicted to exhibit good thermoelectric performance are labelled in bold in Fig. 6(a) and (c). The candidate materials are $AgFeS_2$, $HgCr_2S_4$, $ZnCr_2S_4$, Ag_2FeSnS_4, $NiGa_2S_4$ and NiS. These candidate materials are assessed for their thermoelectric performance in their paramagnetic state, the relevant state at the typical operational temperatures in thermoelectrics.

To model the paramagnetic phase of the candidates, we utilized 5 random samples (RSs) and found sufficiently converged values for total energies and electronic structure parameters, which are presented in Table 1 for both the

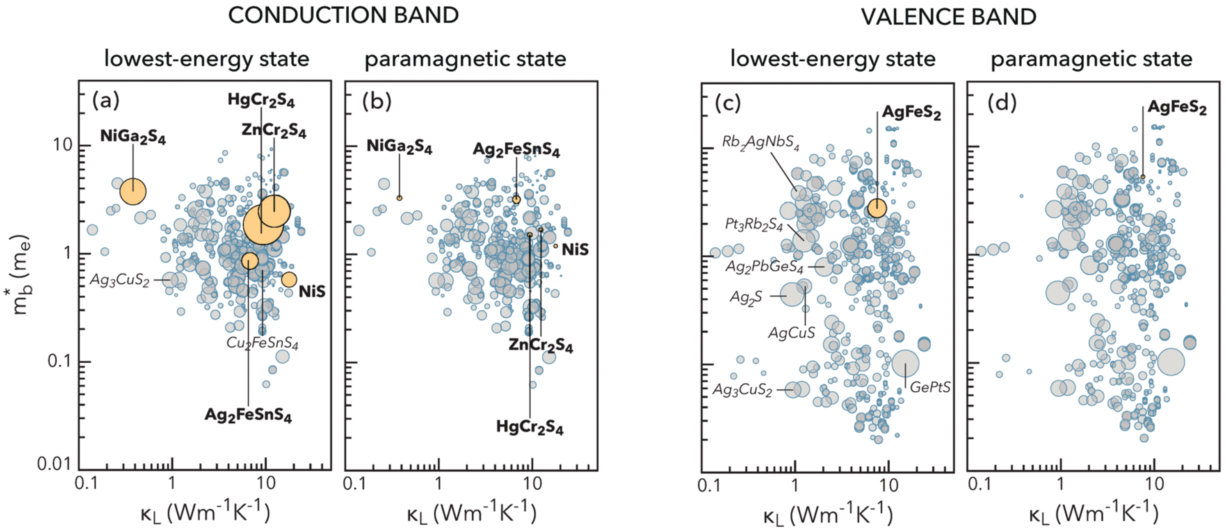

Fig. 6 Calculated β_{SE} as a function of band mass (m_b*) and lattice thermal conductivity (κ_L) of 600 transition-metal sulfides reported in the ICSD, represented by the bubble area for conduction (a and b) and valence (c and d) band transport. Candidate materials that are magnetic in their lowest-energy state are labelled (bold) in the lowest-energy state (a and c) and in the paramagnetic state (b and d). The value of β_{SE} of the candidates decreases significantly from the lowest-energy to the paramagnetic state. Candidates that are non-magnetic are labelled in italics. The value of β_{SE} remains unchanged for non-magnetic candidates.

Table 1 Band gaps (E_g) in eV, valence (VB) and conduction band (CB) DOS effective masses (m_{DOS}*), band degeneracies (N_b), and β_{SE} values in the lowest-energy (GS) and in the paramagnetic (para) state of candidates that are magnetic in GS and labelled in bold in Fig. 6

Candidate		E_g	m_{DOS}* VB, CB	N_b VB, CB	β_{SE} VB, CB
$AgFeS_2$	(GS)	1.1	1.54, 7.01	10, 4	16.5, 1.8
	(para)	0.7	7.08, 10.93	2, 3	0.7, 0.9
Cr_2HgS_4	(GS)	0.4	2.44, 0.02	1.5, 4.5	1.0, 76.3
	(para)	1.1	3.15, 0.93	3, 1	1.0, 2.2
Cr_2ZnS_4	(GS)	1.0	3.30, 0.10	1.5, 6	0.7, 48.0
	(para)	1.3	3.35, 1.15	3, 1	0.7, 1.8
Ag_2FeSnS_4	(GS)	0.7	0.86, 0.03	1, 1.5	1.0, 13.1
	(para)	1.0	5.08, 0.14	2, 1	0.9, 2.9
$NiGa_2S_4$	(GS)	0.9	5.77, 0.38	2, 5.5	1.4, 32.0
	(para)	0.8	2.08, 4.56	0.5, 1.5	0.4, 1.1
NiS	(GS)	0.5	0.90, 3.17	2, 12	1.8, 10.7
	(para)	0.1	1.90, 5.66	2, 2	1.2, 0.6

lowest-energy and the paramagnetic state. Assuming that the lattice thermal conductivity remains unchanged from the lowest-energy state, β_{SE} in the paramagnetic state can be evaluated. Fig. 6(b) and (d) show the equivalent of Fig. 6(a) and (c), respectively, with new β_{SE} values in paramagnetic state for the 6 candidates. We find that for all 6 candidates the predicted thermoelectric performance in the paramagnetic phase is far inferior to that in their lowest-energy state, and as a result the corresponding bubbles in Fig. 6(b) and (d) are small. The ratio of the electronic properties and β_{SE} in the paramagnetic to lowest-energy state are visualized on a parallel coordinate plot in Fig. 7. A value of 1 signifies no change in the property in going from the lowest-energy to the high-T paramagnetic phase. The band gap and degeneracy appear to increase or decrease unsystematically while m_{DOS}* for both the conduction and valence band either remains unchanged or increases in the paramagnetic phase (with the exception of $NiGa_2S_4$ in the VB).

The value of β_{SE} for candidates that are non-magnetic in their lowest-energy state, represented by large bubbles and labelled in italics in Fig. 6(a) and (c), remain unchanged in their high-T state. The electronic structure properties and modeled lattice thermal conductivities along with the β_{SE} values of 16 non-magnetic candidates are presented in Table 2. Most of these candidates are predicted to be better for the valence band or p-type transport. For reference, β_{SE} values for PbTe are ∼15 and ∼17 for the assumed p- and n-type transport, respectively. The range of β_{SE} of the non-magnetic systems exceeds or approaches that of PbTe for GePtS, Ag_2S, Ag_2GePbS_4, $CuNbRb_2S_4$ and $K_3Ag_3Nb_2S_4$ for the p-type (valence band) transport. The conduction band β_{SE} for all of the studied transition-metal sulfides are below that of PbTe. This is mainly due to the presence of the transition metal d-states close to the conduction band edge and relatively high κ_L for the materials where this is not the case. For valence band transport, the presence of Cu and Ag in their +1 nominal oxidation state in high β_{SE} materials helps in increasing the valence band edge dispersion due to repulsion between filled (Cu,Ag)-d and S-p orbitals, and thereby lowering the band effective masses and contributing beneficially to p-type transport. Another interesting feature of the dataset in Table 2 is that all but two compounds contain a group −11 transition metal (Cu, Ag, Au) in combination with V and Nb predominantly in the +5 formal oxidation state with empty d-orbitals contributing to the conduction band. This supports the previous discussion about the apparent

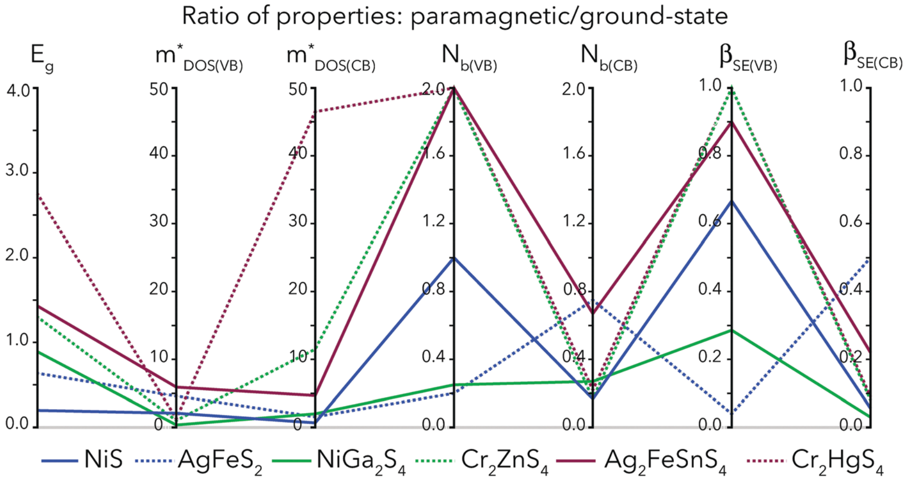

Fig. 7 Parallel coordinate plot of the ratio of different electronic properties in the paramagnetic to lowest-energy state for the 6 candidates shown in Table 1: calculated band gap (E_g) in eV, valence and conduction band density of states effective mass m_{DOS}*, and band degeneracy N_b. The ratio of the value of β_{SE} in the paramagnetic to ground state for valence and conduction band transport are shown on the last two axes.

Table 2 Band gaps (E_g) in eV, valence (VB) and conduction band (CB) DOS effective masses (m_{DOS}*), band degeneracies (N_b), κ_L in W m^{-1} K^{-1}, and β_{SE} values in the ground state of candidates that are non-magnetic

Candidate	E_g	m_{DOS}* VB, CB	N_b VB, CB	κ_L	β_{SE} VB, CB
Ag_2GePbS_4	1.57	1.26, 1.26	6, 2	2.05	16.2, 3.5
Ag_3CuS_2	0.39	1.44, 0.06	4, 1	1.18	11.4, 11.1
$CuNbRb_2S_4$	2.36	7.10, 4.10	13, 3	1.30	14.9, 2.6
Ag_3AuS_2	0.61	0.66, 0.05	2, 1	2.50	7.2, 13.0
Cu_3VS_4	1.36	1.83, 5.10	7, 2	4.60	10.0, 1.0
$K_3Ag_3Nb_2S_4$	2.34	3.70, 7.72	8, 5	0.85	13.6, 4.5
Cu_2RbVS_4	1.45	3.10, 9.70	7, 3	1.60	10.3, 1.6
Cu_3NbS_4	2.0	2.10, 2.60	7, 3	3.90	10.1, 2.6
$AgRb_2VS_4$	1.70	3.50, 7.94	8, 4	1.22	11.8, 2.7
Ag_2CdGeS_4	1.22	2.35, 0.04	3, 1	4.07	3.8, 9.5
Rb_2AgNbS_4	2.50	4.32, 6.07	8, 2	1.09	10.6, 1.3
Fe_2GeS_4	1.50	4.45, 2.26	9, 2	9.55	9.7, 1.8
Ag_7NbVS_6	1.00	6.50, 0.05	4, 1	1.75	4.1, 11.5
AgCuS	0.64	1.25, 0.53	4, 1	1.25	10.4, 2.5
Ag_2S	1.37	2.10, 0.44	10, 1	0.93	26.2, 2.7
GePtS	0.63	0.49, 0.16	9, 2	15.13	34.2, 8.0

asymmetry between the predicted p- and n-type β_{SE} values and potentially raises a concern about electron trapping *i.e.* polaron formation. Using cuprous oxide (Cu_2O) as a model system, hole polarons are not expected to occur for p-type transport in these materials. Our results suggest that among the transition metal sulfides, the following 10 systems: Ag_2GePbS_4, Ag_3CuS_2, $CuNbRb_2S_4$, Cu_3VS_4, $K_3Ag_3Nb_2S_4$, Cu_2RbVS_4 $AgRb_2VS_4$, Rb_2AgNbS_4, AgCuS, and Ag_2S with their $\beta_{SE} > 10$ could be potentially interesting candidates for p-type thermoelectrics.

The absence of any magnetic candidates in the paramagnetic phase among the large β_{SE} transition-metal sulfides considered in this study might be surprising at first. However, this observation resonates with the fact that most known thermoelectric materials that contain transition metals such as iron silicides (FeSi, $FeSi_2$),[45,46] half Heuslers (XNiSn, X = Ti, Zr, Hf),[47,48] skutterudites (Co_4Sb_{12}),[49] and layered oxides ($NaCoO_2$)[50] are non-magnetic in their stoichiometric bulk form. This is supported by our calculations which result in zero-spin for the transition metals in these systems. Highly off-stoichiometric oxides such as $NaCo_{1-x}O_2$[50] and rare-earth doped skutterudites such as $Pr_xCo_4Sb_{12}$[51] do exhibit magnetic behaviour; however, such cases are beyond the scope of this work, which is limited to stoichiometric and chemically-ordered systems. The only example of a good high-temperature thermoelectric material in a paramagnetic phase is $Yb_{14}MnSb_{11}$, which orders ferromagnetically in the ground state and disorders above 50 K.[52] A plausible explanation for why spin disorder at high temperature does not degrade charge transport in $Yb_{14}MnSb_{11}$ is that like other Zintl compounds, the valence and conduction band edges are formed from Sb non-bonding and Sb–Sb anti-bonding orbitals, respectively,[53] and there is no Mn d-orbital contribution to the band edges. In addition, due to the large separation between magnetic Mn atoms (approx. 10), this system approaches the atomic limit in which hopping between sites is suppressed and the spin disorder likely has negligible effect on the electronic structure.

5 Conclusions

In this work, we have demonstrated the importance of including spin disorder in computational materials searches and proposed a computationally-tractable methodology based on the special quasi-random structure to model the paramagnetic phase. We implement this methodology in a high-throughput framework for transition-metal sulfide thermoelectrics. From the materials design point of view, we can conclude that transition metal-containing candidates that are non-magnetic will not suffer from spin disorder-induced degradation of charge transport and therefore, retain the good thermoelectric performance predicted for the ground-state structure. Magnetic candidates are likely to experience deterioration of thermoelectric performance at the relevant high temperatures. While in principle, it is not forbidden to expect candidates that exhibit similar or better thermoelectric performance in the paramagnetic phase, the candidates are expected to be anomalies and therefore, difficult to ''find''. Based on the presented results, it appears that the likelihood of finding good thermoelectric materials among non-magnetic transition metal compounds is higher.

6 Computational details

Creating magnetic SQSs and random samples

The 50–50 binary alloy SQS supercells were generated with the ATAT software package.[54] Instead of using the SQS to model chemical disorder, the 50–50 alloy structure is used to setup the spin-up and spin-down moments on the magnetic atoms such that the net magnetic moment is zero. For CrN and MnSe, we use 48-atom SQS supercells with $\langle \Phi_\alpha \rangle = 0$ for the first seven coordination shells with small non-zero value on the fifth and seventh shell (similar to those used in ref. 34). To check for finite-size effects, we performed the calculations with 64-atom SQS supercells and found that the results are very similar to those obtained with 48-atom supercells. To generate random samples (RSs), supercells with the same number of atoms as the SQS structure were created and the spin-up and spin-down moments were assigned randomly using a random number generator, while keeping the net magnetic moment equal to zero. For each of the case examples, we used 20 different RSs. For thermoelectric screening, 5 RSs were found to give sufficient convergence in the parameters of interest.

DFT+*U* parameters

DFT calculations to compute total energies, volumes, bulk modulus (B) and electronic structure parameters (E_g, m_{DOS}^*, N_b) were performed with the plane-wave VASP code,[55] with the exchange correlation in the Perdew–Burke–Ernzerhof (PBE) functional form within the projector augmented wave (PAW) formalism. For structure relaxations, a procedure similar to that employed in ref. 10 was used, with plane wave cutoffs of 340–400 eV. A suitable on-site correction in the form of Hubbard U in the rotationally invariant form, introduced by Dudarev and coworkers,[56] was applied for transition metals following the methodology in ref. 10 (U = 3 eV for all transition metals, U = 5 eV for Cu and Ag, no U correction for Zn).

To determine the GS ordered magnetic structure, we performed a limited search by enumerating over all possible magnetic configurations on a primitive unit cell. In the case of CrN and MnSe, we performed this search on a (111) supercell containing twice the number of atoms in the primitive cell, which is required to realize the known AFM GS. Because the number of magnetic configurations scales as 2^N with the number of magnetic atoms (N), we limited the total number of enumerations to a maximum of 32, corresponding to all magnetic configurations on a structure containing 6 or less magnetic atoms per unit cell. For example, Fe_3O_4 contains 6 Fe atoms in the primitive cell, where one of the 32 configurations considered corresponds to the known ferrimagnetic order.

Calculation of m_{DOS}^* and N_b was undertaken on a dense k-point grid with a fixed number of k-points per atom, as determined by the equation $N_{atoms} \times N_{kpts} = 8000$, where N_{atoms} is the number of atoms in the primitive cell and N_{kpts} the number of k-points. B is calculated by fitting the Birch–Murnaghan equation of state[57] to a set of total energies computed at different volumes. m_{DOS}^* is determined from the electronic DOS within a parabolic band approximation, such that the parabolic band reproduces the same number of states as the computed DOS within a 100 meV (adjustable) energy window from the relevant band edge.

Acknowledgements

We acknowledge support from NSF DMR program, grant no. 1334713. This work was supported in part by the US Department of Energy under contract no. DE-AC36-08GO28308 to NREL and through NREL's LDRD program under grant no. 06591403. The research was performed using computational resources sponsored by the Department of Energy's Office of Energy Efficiency and Renewable Energy and located at the NREL.

References

1 T. Connolly and E. D. Copenhaver, *Bibliography of Magnetic Materials*, Springer US, 1972.
2 J. M. D. Coey, *Magnetism and Magnetic Materials*, Cambridge University Press, 2010.
3 G. J. Snyder and E. S. Toberer, *Nat. Mater.*, 2008, **7**, 105–114.
4 E. Skoplaki and J. Palyvos, *Renewable Energy*, 2009, **34**, 23–29.
5 A. Jain, S. P. Ong, G. Hautier, W. Chen, W. D. Richards, S. Dacek, S. Cholia, D. Gunter, D. Skinner, G. Ceder and K. A. Persson, *APL Mater.*, 2013, **1**, 011002.
6 S. Curtarolo, W. Setyawan, S. Wang, J. Xue, K. Yang, R. H. Taylor, L. J. Nelson, G. L. Hart, S. Sanvito, M. Buongiorno-Nardelli, N. Mingo and O. Levy, *Comput. Mater. Sci.*, 2012, **58**, 227–235.
7 J. Saal, S. Kirklin, M. Aykol, B. Meredig and C. Wolverton, *JOM*, 2013, **65**, 1501–1509.
8 S. Lany, *J. Phys.: Condens. Matter*, 2015, **27**, 283203.
9 S. Lany, *Phys. Rev. B: Condens. Matter Mater. Phys.*, 2013, **87**, 085112.
10 V. Stevanović, S. Lany, X. Zhang and A. Zunger, *Phys. Rev. B: Condens. Matter Mater. Phys.*, 2012, **85**, 115104.
11 A. Filippetti, W. E. Pickett and B. M. Klein, *Phys. Rev. B: Condens. Matter Mater. Phys.*, 1999, **59**, 7043–7050.
12 D. E. Jiang and E. A. Carter, *Phys. Rev. B: Condens. Matter Mater. Phys.*, 2003, **67**, 214103.
13 V. P. Antropov, M. I. Katsnelson, B. N. Harmon, M. van Schilfgaarde and D. Kusnezov, *Phys. Rev. B: Condens. Matter Mater. Phys.*, 1996, **54**, 1019–1035.
14 Y. Kakehashi, S. Akbar and N. Kimura, *Phys. Rev. B: Condens. Matter Mater. Phys.*, 1998, **57**, 8354–8369.

15 R. Drautz and M. Fähnle, *Phys. Rev. B: Condens. Matter Mater. Phys.*, 2004, **69**, 104404.

16 A. Franceschetti, S. V. Dudiy, S. V. Barabash, A. Zunger, J. Xu and M. van Schilfgaarde, *Phys. Rev. Lett.*, 2006, **97**, 047202.

17 P.-W. Ma, W. C. Liu, C. H. Woo and S. L. Dudarev, *J. Appl. Phys.*, 2007, **101**, 073908.

18 M. Eisenbach, D. Perera, D. P. Landau, D. M. Nicholson, J. Yin and G. Brown, *J. Phys.: Conf. Ser.*, 2015, **640**, 012019.

19 A. Zunger, S.-H. Wei, L. G. Ferreira and J. E. Bernard, *Phys. Rev. Lett.*, 1990, **65**, 353–356.

20 J. Yan, P. Gorai, B. Ortiz, S. Miller, S. A. Barnett, T. Mason, V. Stevanović and E. S. Toberer, *Energy Environ. Sci.*, 2015, **8**, 983–994.

21 D. Gall, C.-S. Shin, R. T. Haasch, I. Petrov and J. E. Greene, *J. Appl. Phys.*, 2002, **91**, 5882–5886.

22 X. Y. Zhang, J. S. Chawla, R. P. Deng and D. Gall, *Phys. Rev. B: Condens. Matter Mater. Phys.*, 2011, **84**, 073101.

23 A. S. Botana, F. Tran, V. Pardo, D. Baldomir and P. Blaha, *Phys. Rev. B: Condens. Matter Mater. Phys.*, 2012, **85**, 235118.

24 A. S. Botana, V. Pardo, D. Baldomir and P. Blaha, *Phys. Rev. B: Condens. Matter Mater. Phys.*, 2013, **87**, 075114.

25 V. I. Anisimov and A. V. Lukoyanov, *Acta Crystallogr., Sect. C: Struct. Chem.*, 2014, **70**, 137–159.

26 G. Kotliar and D. Vollhardt, *Phys. Today*, 2004, **57**, 53–59.

27 I. Abrikosov, A. Ponomareva, P. Steneteg, S. Barannikova and B. Alling, *Curr. Opin. Solid State Mater. Sci.*, 2016, **20**, 85–106.

28 V. P. Antropov, M. I. Katsnelson, M. van Schilfgaarde and B. N. Harmon, *Phys. Rev. Lett.*, 1995, **75**, 729–732.

29 V. P. Antropov, M. I. Katsnelson, B. N. Harmon, M. van Schilfgaarde and D. Kusnezov, *Phys. Rev. B: Condens. Matter Mater. Phys.*, 1996, **54**, 1019–1035.

30 B. L. Gyorffy, A. J. Pindor, J. Staunton, G. M. Stocks and H. Winter, *J. Phys. F: Met. Phys.*, 1985, **15**, 1337–1386.

31 B. Alling, T. Marten, I. A. Abrikosov and A. Karimi, *J. Appl. Phys.*, 2007, **102**, 044314.

32 A. V. Ruban and V. I. Razumovskiy, *Phys. Rev. B: Condens. Matter Mater. Phys.*, 2012, **85**, 174407.

33 G. Rushbrooke and P. Wood, *Mol. Phys.*, 1958, **1**, 257–283.

34 B. Alling, T. Marten and I. A. Abrikosov, *Phys. Rev. B: Condens. Matter Mater. Phys.*, 2010, **82**, 184430.

35 C. Jiang, C. Wolverton, J. Sofo, L.-Q. Chen and Z.-K. Liu, *Phys. Rev. B: Condens. Matter Mater. Phys.*, 2004, **69**, 214202.

36 Z. W. Lu, S.-H. Wei and A. Zunger, *Phys. Rev. B: Condens. Matter Mater. Phys.*, 1992, **45**, 314–330.

37 S.-H. Wei, L. G. Ferreira and A. Zunger, *Phys. Rev. B: Condens. Matter Mater. Phys.*, 1992, **45**, 2533–2536.

38 M. Sanati, G. L. W. Hart and A. Zunger, *Phys. Rev. B: Condens. Matter Mater. Phys.*, 2003, **68**, 155210.

39 A. van de Walle, P. Tiwary, M. de Jong, D. Olmsted, M. Asta, A. Dick, D. Shin, Y. Wang, L.-Q. Chen and Z.-K. Liu, *Calphad*, 2013, **42**, 13–18.

40 K. E. Ingle, J. B. C. Efrem D'sa, A. Das and K. R. Priolkar, *J. Magn. Magn. Mater.*, 2013, **347**, 68–71.

41 P. Gorai, P. Parilla, E. S. Toberer and V. StevanovicĞ, *Chem. Mater.*, 2015, **27**, 6213–6221.

42 R. P. Chasmar and R. Stratton, *J. Electron. Control*, 1959, **7**, 52–72.

43 A. Belsky, M. Hellenbrandt, V. L. Karen and P. Luksch, *Acta Crystallogr., Sect. B: Struct. Sci.*, 2002, **58**, 364–369.

44 P. Gorai, D. Gao, B. Ortiz, S. Miller, S. Barnett, T. Mason, Q. Lv, V. Stevanovic and E. S. Toberer, *Comput. Mater. Sci.*, 2016, **112**, 368–376.

45 M. Neef, K. Doll and G. Zwicknagl, *J. Phys.: Condens. Matter*, 2006, **18**, 7437–7447.

46 Z. Schlesinger, Z. Fisk, H.-T. Zhang, M. B. Maple, J. DiTusa and G. Aeppli, *Phys. Rev. Lett.*, 1993, **71**, 1748–1751.

47 C. Felser and A. Hirohata, *Heusler Alloys*, Springer, 2016.

48 K. Ahilan, M. C. Bennett, M. C. Aronson, N. E. Anderson, P. C. Canfield, E. Munoz-Sandoval, T. Gortenmulder, R. Hendrikx and J. A. Mydosh, *Phys. Rev. B: Condens. Matter Mater. Phys.*, 2004, **69**, 245116.

49 H. Anno, K. Hatada, H. Shimizu, K. Matsubara, Y. Notohara, T. Sakakibara, H. Tashiro and K. Motoya, *J. Appl. Phys.*, 1998, **83**, 5270–5276.

50 G. Lang, J. Bobroff, H. Alloul, P. Mendels, N. Blanchard and G. Collin, *Phys. Rev. B: Condens. Matter Mater. Phys.*, 2005, **72**, 094404.

51 K. Tanaka, Y. Sekihara, Y. Kawahito, D. Kikuchi, H. Aoki, K. Kuwahara, Y. Aoki, H. Sugawara and H. Sato, *J. Magn. Magn. Mater.*, 2007, **310**, 1715–1717.

52 J. F. Rauscher, C. A. Cox, T. Yi, C. M. Beavers, P. Klavins, E. S. Toberer, G. J. Snyder and S. M. Kauzlarich, *Dalton Trans.*, 2010, **39**, 1055–1062.

53 J. Xu and H. Kleinke, *J. Comput. Chem.*, 2008, **29**, 2134–2143.

54 A. van de Walle, M. Asta and G. Ceder, *Calphad*, 2002, **26**, 539–553.

55 G. Kresse and J. Furthmüller, *Phys. Rev. B: Condens. Matter Mater. Phys.*, 1996, **54**, 11169–11186.

56 S. L. Dudarev, G. A. Botton, S. Y. Savrasov, C. J. Humphreys and A. P. Sutton, *Phys. Rev. B: Condens. Matter Mater. Phys.*, 1998, **57**, 1505–1509.

57 F. Birch, *J. Geophys. Res.*, 1952, **57**, 227–286.